Title: A Catalyst-like System Enables Efficient Perovskite Solar Cells

Yuqian Yang[1†], Guodong Li[2,10†], Lichen Zhao[3†], Pengju Tan[1], Yu Li[4], Shunde Li[3], Lina Tan[2], Chunyan Deng[2], Shibo Wang[2], Zhenzhu Zhao[1], Chengjian Yuan[1], Honghe Ding[4], Liang Chen[4], Junfa Zhu[4], Yong Guan[4], Cheng-Hung Hou[6], Pengyi Tang[7], Quiyang Li[3], Hong Liu[7], Yingguo Yang[5], Antonio Abate[8], Jing-Jong Shyue[6], Jihuai Wu[2*], Thomas P. Russell[9], Qin Hu[1*]*

[1]School of Microelectronics, University of Science and Technology of China, Hefei, Anhui 230026, China.

[2]Engineering Research Center of Environment-Friendly Functional Materials, Ministry of Education, Fujian Provincial Key Laboratory of Photoelectric Functional Materials, Institute of Materials Physical Chemistry, Huaqiao University, Xiamen 361021, China.

[3]State Key Laboratory for Artificial Microstructure and mesoscopic Physics, School of Physics, Frontiers Science Center for Nano-optoelectronics & Collaborative Innovation Center of Quantum Matter, Peking University, Beijing 100871, China.

[4]National Synchrotron Radiation Laboratory (NSRL), University of Science and Technology of China, Hefei, Anhui 230029, China.

[5]Shanghai Synchrotron Radiation Facility (SSRF), Zhangjiang Lab, Shanghai Advanced Research Institute, Chinese Academy of Sciences, Shanghai 201204, China.

[6]Research Center for Applied Sciences, Academia Sinica, Taipei 11529, Taiwan.

[7]State Key Laboratory of Information Functional Materials, 2020 X-Lab, ShangHai Institute of Microsystem and Information Technology, Chinese Academy of Sciences, Shanghai 200050, China.

[8]Department Novel Materials and Interfaces for Photovoltaic Solar Cells Helmholtz-Zentrum Berlin für Materialien und Energie Kekuléstraße 5, 12489 Berlin, Germany.

[9]Polymer Science and Engineering Department, Conte Center for Polymer Research, University of Massachusetts, 120 Governors Drive, Amherst, MA 01003, USA.
[10]Institute of Carbon Neutrality and New Energy, School of Electronics and Information, Hangzhou Dianzi University, Hangzhou 310018, China

†These authors contributed equally to this work.
E-mail: qinhu20@ustc.edu.cn; yli1@ustc.edu.cn; jhwu@hqu.edu.cn
Keywords: Perovskite solar cells; Formation kinetics; Catalyst-like system; Homogeneity; Multiscale structure

Abstract

High-quality perovskite films are essential for achieving high performance of optoelectronic devices. However, solution-processed perovskite films are known to suffer from compositional and structural inhomogeneity due to lack of control over the kinetics during the formation. Here, we successfully enhanced the microscopic homogeneity of perovskite films by modulating the conversion reaction kinetics using a catalyst-like system generated by a foaming agent. The chemical and structural evolution during this catalytic conversion was revealed by a multimodal synchrotron toolkit with spatial resolutions spanning many length scales. Combining these insights with simulations, a cyclic conversion pathway model was developed that yielded exceptional perovskite homogeneity due to enhanced conversion, having a power conversion efficiency of 24.45% for photovoltaic devices. Our work establishes a systematic link between processing of precursor and homogeneity of the perovskite films.

1. Introduction

Metal halide perovskites have demonstrated an unprecedented success in photovoltaics, photodetectors and light emitting diodes (LEDs) due to their excellent optoelectronic properties[1]. The quality of perovskite films plays a pivotal role in determining device performance[2, 3]. Among diverse perovskite preparation methods, solution-based deposition holds a beautiful prospect for future commercialization due to cost-effective processing[2, 4]. Nevertheless, solution-processed perovskite films often suffer from inhomogeneities, including structural disorder, pinholes, and PbI_2 inclusions, that function as traps for photoexcited carriers, leading to diminished performance through non-radiative recombination[5]. This trapping process also initiates photochemical degradation in the absorber layer, collectively contributing to the device's compromised efficiency and stability[6]. These undesirable inhomogeneous states, are generally unavoidable, due to competing and uncontrollable processing kinetics involved in the fabrication process[7].

Mass transport is a crucial aspect of perovskite conversion as it involves the movement of reactants and products within the film, which can help to mitigate inhomogeneity in the final product[4, 8]. Factors that affect mass transport during this process include the size and morphology of PbI_2 crystals, precursor solution concentration and diffusion, and the presence of additives or surfactants[4, 9]. Attempts have been made to manipulate PbI_2 structure to enhance the transport of ammonium salts and facilitate perovskite formation, such as the post-treatment[10], additive control[4] and low-dimensional engineering[11]. Recently, the impact of PbI_2 microstructure on mass transport during perovskite conversion was verified theoretically and experimentally, which is applicable to high-efficiency perovskite solar cells (PSCs)[12].

Despite these advances in mass transport[4, 13], achieving high-quality perovskite films remains a challenge in conventional reaction pathways. The coordination between PbI_2 and polar solvents is known to form intermediate phases during perovskite

conversion[14, 15]. Various volatile intermediates, such as PbI_2-methyl sulfoxide (DMSO)[15], PbI_2-4-tert-butylpyridine[16] and PbI_2-N-methyl-2-pyrrolidone[4], have been utilized to optimize the reaction pathway. While these intermediates can improve the crystal quality of perovskite films, the volume reduction resulting from solvent evaporation during annealing can lead to the formation of pinholes. Alternative pathways based on non-volatile intermediates have been proposed[17]. For example, a solid-state cesium acetate was introduced to induce recrystallization of the perovskite[18]. Methylamine formate was adopted for robust transformation to perovskite[19]. Nevertheless, incomplete transformation remains inevitable, as the solid–liquid reaction encounters challenges in propagating from PbI_2 surfaces to the inner regions, due to the consumption of intermediates[7, 20]. Given this scenario, the development of reaction pathways that enable improved utilization of intermediates is crucial for achieving thorough phase conversion and producing high-quality perovskite.

In this work, we first elucidated a cyclic reaction pathway during two-step perovskite conversion, enabled by catalytic PbI_2-mesylate anion (MeS^-) complexes. By combining *in-situ* grazing incidence wide-angle X-ray scattering (GIWAXS) with nano-computed tomography (nano-CT) and synchrotron radiation photoemission spectroscopy (SRPES), the structural and compositional properties evolution during conversion from PbI_2 complexes to resulting perovskite were elucidated over multiple scales (micro/nanoscale) and dimensions. Our findings demonstrate that the formation of MeS^- within the multi-scale PbI_2 framework through a foaming reaction triggers a catalytic process characterized by low energy barriers and enhanced mass transport, thereby reducing the occurrence of pinholes and PbI_2 inclusions. Benefiting from the compositional and structural homogeneity of the perovskite film, the corresponding PSC had a PCE of 24.45% and excellent long-term stability. Our work presents a novel catalyst-like strategy for regulating the kinetics of perovskite reaction.

2. Results and discussion

2.1 Chemical mechanism of PbI_2 complexes formation

In an attempt to manipulate the reaction pathways, we introduced Methanesulfonohydrazide (MeSH) into the PbI_2 precursor. MeSH is a widely used chemical foaming agent with good solubility and non-volatile nature[21]. The top-view scanning electron microscope (SEM) images of PbI_2 complexes are showed in Figure 1A and 1B, where potential porous regions are outlined in Figure S1 by a plugin of PyPIE software, Particle Counter[22]. It is evident that the MeSH-based PbI_2 complexes (denoted as Target-PbI_2) shows higher pore densities from larger pore counts and porous area ratios than the control sample (denoted as Control-PbI_2) at nanoscale levels (10-100 nm). However, Target-PbI_2 transforms into a pore-free perovskite film (denoted as Target-PVSK) (Figure 1D and Figure S1G), while Control-PbI_2 transforms to an inferior perovskite film (denoted as Control-PVSK) containing pinholes (Figure 1C and Figure S1H). These results suggest that the MeSH inclusion has a distinct impact on the morphology of both the PbI_2 and resulting perovskite film.

To understand the chemical reaction mechanism during the PbI_2 formation process, we performed Fourier transform infrared spectroscopy (FTIR) on pure MeSH, Control-PbI_2 and Target-PbI_2 before and after 70 °C annealing (Figure 1E and S2). The spectrum of pure MeSH shows peaks of asymmetric (1146 cm^{-1}) and symmetric (1330 and 1304 cm^{-1}) stretching vibrations from S=O[23]. Before annealing, Target-PbI_2 closely resembles Control-PbI_2, except for an additional peak of S=O from MeSH at 1159 cm^{-1}, suggesting minimal influence from MeSH on PbI_2. For Target-PbI_2 after annealing, these peaks shift to 1158 cm^{-1} and 1340 cm^{-1}, with a new peak emerging at 1047 cm^{-1}, attributed to the S=O stretching vibration from the $-SO^{3-}$ ions[24]. There are no N-H stretching vibration (3370 cm^{-1}) detected for Target-PbI_2. ^1H NMR spectra were obtained from the samples prepared by dissolving MeSH and PbI_2-MeSH in DMSO-d_6 solvent before and after heating at 70 ℃ (Figure 1F). The corresponding positions of H are identified in Figure S2[25]. The H signal assigned to $-CH_3$ from $CH_3SO_3^-$ (Peak 4 in Figure 1F, denoted as MeS^-) is intensified after heating,

especially for PbI_2-MeSH. According to the ratios of integrated peak areas (1/3Peak4 : Peak1) in Figure S4A, PbI_2-MeSH shows a larger value after heating, indicating that the presence of more MeS^-. In Figure S4B, it is observed that Peak 4 in PbI_2-MeSH shifts downfield after heating, while the peak of pure MeSH remains unchanged, due to the shielding effect induced by Pb^{2+} ions[26]. In the density functional theory (DFT) calculation (Figure S5), MeS^- as a Lewis base can attract Pb^{2+} with a binding energy of −0.68 eV, further validating the generation of PbI_2-MeS^- complexes, although not preferentially compared to the solvent intermediates. The gas chromatography-mass spectrometry (GC–MS) of MeSH during heating process is shown in Figure S6. The gas chromatography (Figure S6A) shows a main chromatographic peak near the retention time of 1.94 minutes. According to the corresponding mass spectrum (Figure S6B), the m/z value of the main fragment is 28, indicating the release of nitrogen (N_2). This confirms the existence of -SO^{3-} and absence of -N-H in PbI_2, since MeSH, serving as a foaming agent, undergoes thermal decomposition during annealing, releasing N_2 gases in what is termed the foaming reaction. By considering the electrostatic potential of MeSH molecule (Figure S7), it can be deduced that the amine groups (−$NHNH_3$) transform into gas upon heating, and the negative part (−CH_3SO_2) turns into MeS^- after the foaming reaction. The vertical compositional profiles of Control-PbI_2 and Target-PbI_2 were validated using time-of-flight secondary ion mass spectrometry (ToF-SIMS). Given the similar I^- and InO_2− profiles shown in Figure 1G, a pronounced signal of MeS^- component is identified in Target-PbI_2 while Control-PbI_2 shows a barely detected MeS^- signal. The SRPES (Figure S8, A-C) further confirms the existence of MeS^- in Target-PbI_2, since it exhibits an additional C 1s peak of the C−S bond[26] and a strong S 2p peak assigned to −C−SO_3^-[27]. As expected, there is no N 1s signal for Target-PbI_2 due to the complete release of gas during thermal decomposition. Accordingly, we propose the corresponding formation process of PbI_2-MeS^- complexes through foaming reaction (Figure 1H). Benefitting from bubble stretching, the PbI_2 framework shows increased porosity, accompanied by the formation of MeS^--based complexes.

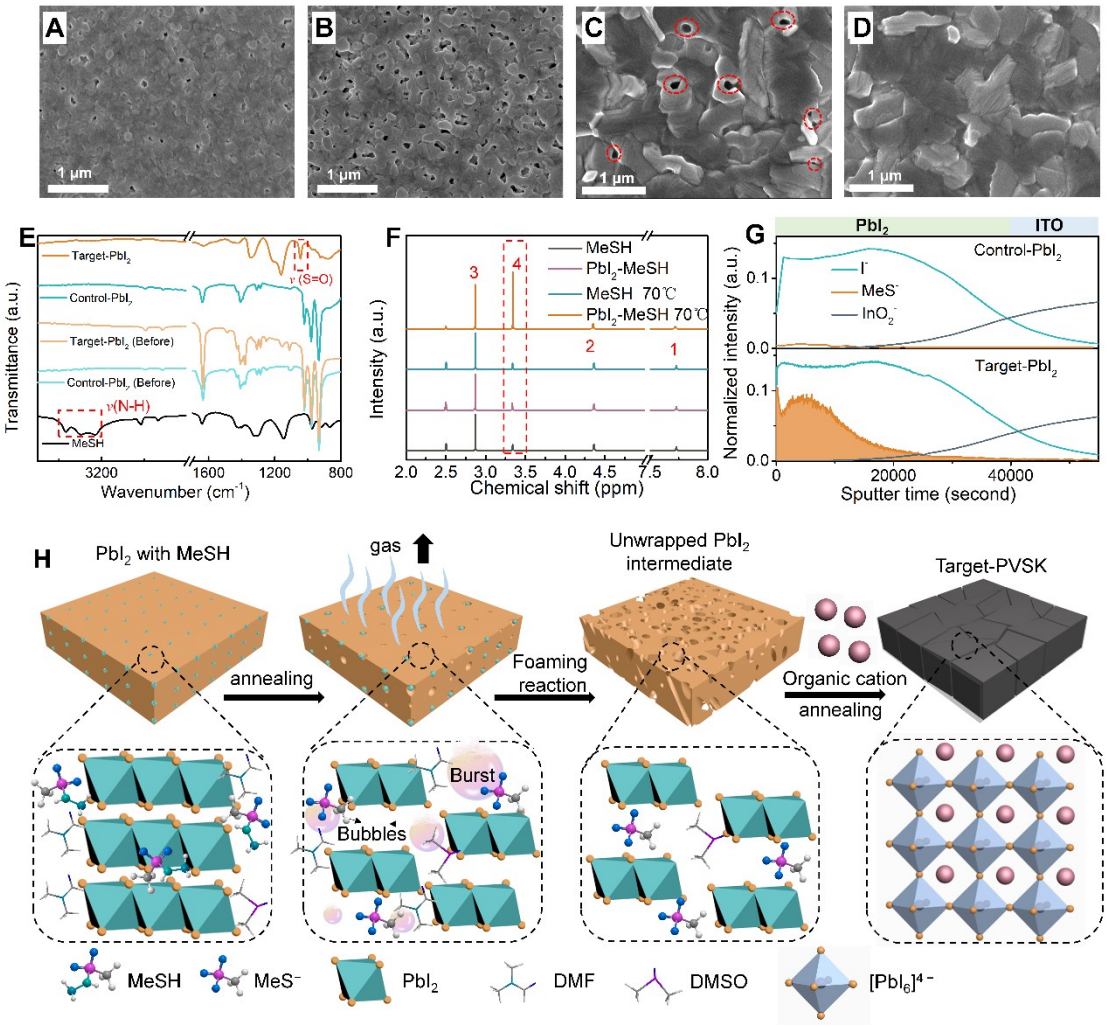

Figure 1. The formation mechanism of the PbI_2 complexes assisted by the foaming agent. (**A**-**B**) Top-view SEM images of PbI_2 and perovskite films without and with MeSH inclusion. (**A**) Control-PbI_2, (**B**) Target-PbI_2, (**C**) Control-PVSK, (**D**) Target-PVSK. (**E**) FTIR spectra of pure MeSH, Control-PbI_2 and Target-PbI_2 before and after annealing. The red dotted lines mark the characteristic peaks of S=O and N-H. (**F**) ^{1}H liquid-state NMR spectra of MeSH and PbI_2-MeSH before and after heating at 70 ℃. The numbers correspond to the different types of H in Figure S3, the dotted box marks the H signal of -CH_3 from $CH_3SO_3^-$ (Peak 4). (**G**) ToF-SIMS measurements of Control-PbI_2 and Target-PbI_2 on ITO substrates. h, Schematic illustrations of the formation processes of foamed PbI_2 and perovskite.

2.2 Formation evolution and microstructure of PbI_2 complexes

We then carried out GIWAXS measurements to clarify the formation kinetics of PbI_2 complexes in nanoscale. Figure 2A-2D shows the *in-situ* GIWAXS snapshots of Control-PbI_2 and Target-PbI_2 at the beginning (10 s) and end (325 s) of the annealing process. At 10 s, both diffraction patterns are similar with peaks at ~ 0.7 $Å^{-1}$ and ~ 0.9 $Å^{-1}$, which can be attributed to the solvent complex (PbI_2-N,N-dimethylformamide (DMF) or PbI_2-DMSO)[4, 28] and (001) planes of the PbI_2 crystal, respectively[29]. Control-PbI_2 exhibits a lower abundance of the hexagonal PbI_2 phase due to the strong coordination interaction between PbI_2 and the solvents (DMSO and DMF). At 325 s, however, Target-PbI_2 (Figure 2D) shows a notably intense signal from the PbI_2 phase in comparison with Control-PbI_2 (Figure 2C). We further recorded the evolution of scattering intensities during annealing as shown in Figure 2E, 2F and S9. Scattering from the PbI_2 complex is attenuated slowly as the solvent evaporates[30], while scattering from the (001) plane remains weak and shows no noticeable change. With the participation of MeSH, the features in Target-PbI_2 sample change abruptly at ~ 190 s, when the (001) plane peak (q~ 0.9 $Å^{-1}$) starts intensifying along with the subsidence of the solvent complex. These differences of nanoscale phase components are attributed to the large surface area of the porous structure, which facilitates solvent evaporation and PbI_2 formation.

The three-dimensional (3D) microstructures of the resulting PbI_2 complexes were studied via synchrotron X-ray nano-CT (Figure 2G and 2H), a non-destructive 3D imaging technology with high spatial resolutions. The structure with holes through the entire film is easily distinguishable from the PbI_2 matrix (see Movie S1 and Movie S2 for more details). In Figure S10, A and B, the pores in Target-PbI_2 are multiscale and unevenly distributed compared to Control-PbI_2. The cross-sectional images and corresponding extracted cross-sectional profiles are shown in Figure S10, C and D. MeSH induces more uneven profiles, which could benefit superior permeation for the amine-salt solution. Combining the finding from microscopic images, we verify the multiscale pores architecture of PbI_2 complexes, which is schematically depicted in

Figure S11. Target-PbI_2 shows a well-connected pore structure, which improve the diffusion and reactivity of reactants in the subsequent conversion reaction.

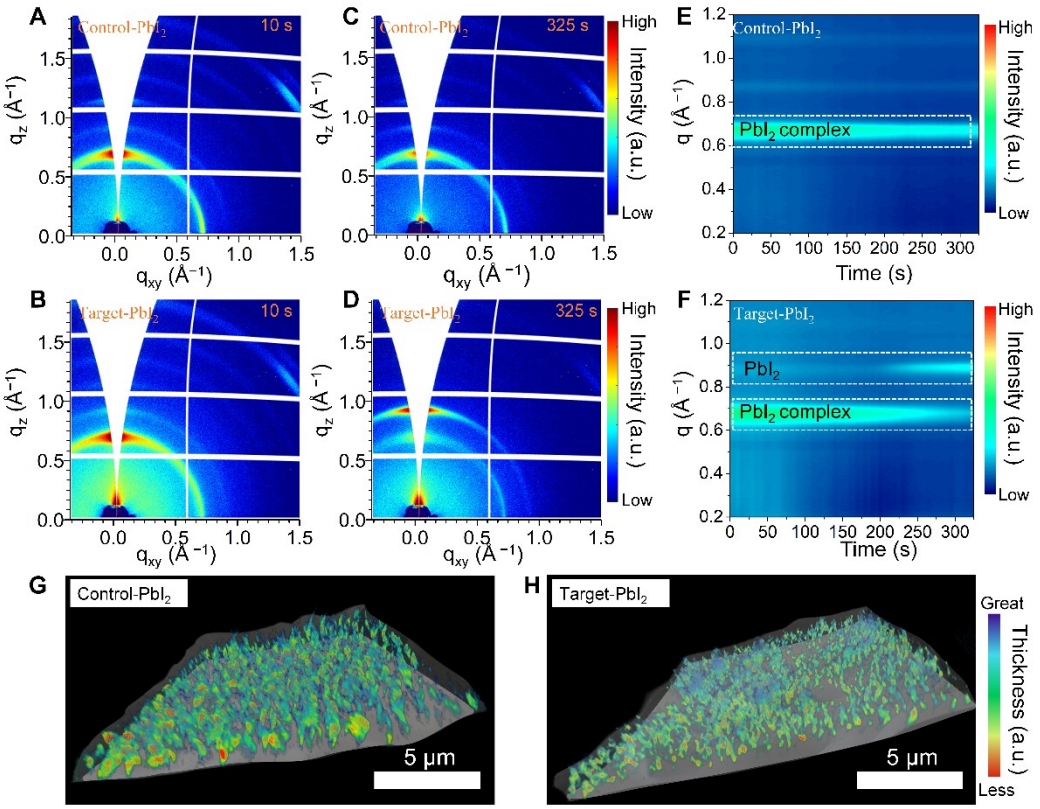

Fig. 2. The formation process and 3D structure visualization of PbI_2 complexes. (**A**-**F**) GIWAXS profile of the formation of Control-PbI_2 (**A**, **C** and **E**) and Target-PbI_2 (**B**, **D** and **F**) during the annealing process. (**A**-**D**), Azimuthally integrated 2D GIWAXS snapshots at 10 s and 325 s, respectively. (**E, F**) The corresponding X-ray scattering intensity evolution during the annealing process. (**G, H**) 3D-reconstructed microstructure of Control-PbI_2 (**G**) and Target-PbI_2 (**H**) via nano-CT.

2.3 Conversion evolution and mechanism of perovskite

In-situ GIWAXS was adopted to study the phase evolution of perovskite formation (Figure 3A-3F). The integrated line profiles in Figure 3A and 3B clearly indicate distinct trends for Control-PVSK and Target-PVSK as a function of annealing time. Figure S12 presents the in-situ 2D GIWAXS patterns of Control-PVSK and Target-

PVSK taken at 0 s, 200 s, and 325 s during the annealing process, respectively, showing the distinct peak characteristics of PbI_2 and perovskite. The corresponding false-color intensity maps are illustrated in Figure 3C and 3D as a function of annealing time, and Figure S13 provides the in-situ temperature curves. Three stages are identified during this process: I) intermediate phases, II) intermediate conversion to perovskite and III) perovskite phase stabilization stage. In Stage I, scattering peaks at 0.45-0.65 $Å^{-1}$, assigned to the DMSO-intermediate (FAI-PbI_2-DMSO)[31], are present for Control-PVSK and Target-PVSK (Figure 3C and 3D). These peaks then vanish with increasing annealing time. Notably, both samples exhibit dominance of the δ-phase perovskite (q~ the δ-phase perovskite (~ 0.81 $Å^{-1}$)[32] in Stage I and then gradually fades away in Stage II. Then the peak intensity of δ-$FAPbI_3$ as the main intermediate gradually decreases in Stage II as the peak intensity of perovskite gradually increases in Control-PVSK. However, a new scattering (~ 0.83 $Å^{-1}$) appears at approximately 135 s in Target-PVSK (Figure 3D), belonging to a MeS^--related intermediate. In Figure S14, the X-ray diffraction patterns of Target-PVSK reveal two prominent peaks at11.6° (0.82 $Å^{-1}$) and 12.0° (0.85 $Å^{-1}$), which are indicative of the presence of the δ-phase and MeS^--related intermediates. More details of the phase conversion are provided in Figures 3E and 3F, where the time evolution of the scattering intensities of the reaction products is shown. For Control-PVSK (Figure 3E), the subsidence of the δ-$FAPbI_3$ corresponds to the enhancement of the perovskite peak (~ 0.96 $Å^{-1}$) in Stage II, suggesting a possible direct conversion from the conventional intermediate to perovskite. Therefore, the following reaction is considered[33]:

$$\text{FAI-PbI}_2\text{-DMSO} \rightarrow \delta\text{-FAPbI}_3 + \text{DMSO}\uparrow \rightarrow \alpha\text{-FAPbI}_3 \quad (1)$$

However, Target-PVSK shows a distinct evolution trend (Figure 3F), characterized by a rapid increase in perovskite peak intensity compared to the slow decrease in the δ-$FAPbI_3$ peak intensity. This suggests a more efficient phase conversion process dominated by the MeS^- intermediate (marked in Figure 3D). Interestingly, the MeS^--intermediate keeps a dynamic growth together with the increasing α-$FAPbI_3$ and decreasing δ-$FAPbI_3$ in Stage II-1. This also indicates that the non-volatile MeS^- ions

remain in the film in this stage without removal along with the DMSO molecule. Otherwise, the intensity of the MeS^--intermediate will also decrease since the rate of perovskite formation is much more rapid than δ-$FAPbI_3$ decomposition. In Stage II-2, the δ-$FAPbI_3$ completely vanishes, and the MeS^--intermediate weakens gradually as the conversion of perovskite reaches completion. In Stage III, the perovskite diffraction in both films attenuates slightly, attributed to degradation under long-time annealing at a temperature of 150 °C[34]. The perovskite conversion with MeSH is terminated at 265 s, which is faster than the control counterpart (at 300 s), indicating more efficient conversion. The relative phase fractions of the final perovskite film (Figure S15) reveal the presence of PbI_2 resulting from the degradation of perovskite in both samples, mainly caused by the inadequate atmosphere in the home-built glove box during the GIWAXS experiment. The target sample shows a significantly lower PbI_2 ratio, indicating reduced residual PbI_2.

The more efficient perovskite conversion with MeSH is supported by DFT calculations. In order to simplify the calculation model, we selected $FAPbI_3$ as the perovskite composition and omitted MACl, DMSO and DMF as they have volatilized away during perovskite annealing. The results in Figure 3G illustrate the MeS^--induced reaction pathway and the energy barriers via the climbing image nudged elastic band (CI-NEB) method. The direct conversion between PbI_2 and FAI requires overcoming a high energy barrier of 0.64 eV (Figure 3G). However, by introducing MeS^-, the reaction is processed in three steps. The energy barrier for the first step, the formation of PbI_2-MeS^- complexes, is reduced to 0.57 eV. 0.43 eV is required for the reaction between FAI and PbI_2-MeS^-, and 0.58 eV for the final conversion of the perovskite phase. Based on our results, the mechanism for MeS^--driven perovskite conversion is proposed:

$$PbI_2 + MeS^- \rightarrow PbI_2\text{-}MeS^- \quad (2)$$

$$FAI + PbI_2\text{-}MeS^- \rightarrow FAPbI_3\text{-}MeS^- \quad (3)$$

$$FAPbI_3\text{-}MeS^- \rightarrow FAPbI_3 + MeS^- \quad (4)$$

From Figure S16, it is observed that the MeS^- is released instead of being coordinated with perovskite due to its the low free energy. The released MeS^- can coordinate with

PbI_2 again to form PbI_2-MeS^-, which then participate in the next round of the conversion reaction of equations (2)-(4). This cyclic reaction pathway is in agreement with the presence of the MeS^- species deduced from Figure 3F. Based on this understanding, the perovskite conversion mechanism is illustrated in Figure 3H, wherein MeS^- acts like a catalyst induces the cyclic reaction pathway. This mechanism promotes efficient perovskite conversion and grain growth by reducing the

energy barriers.

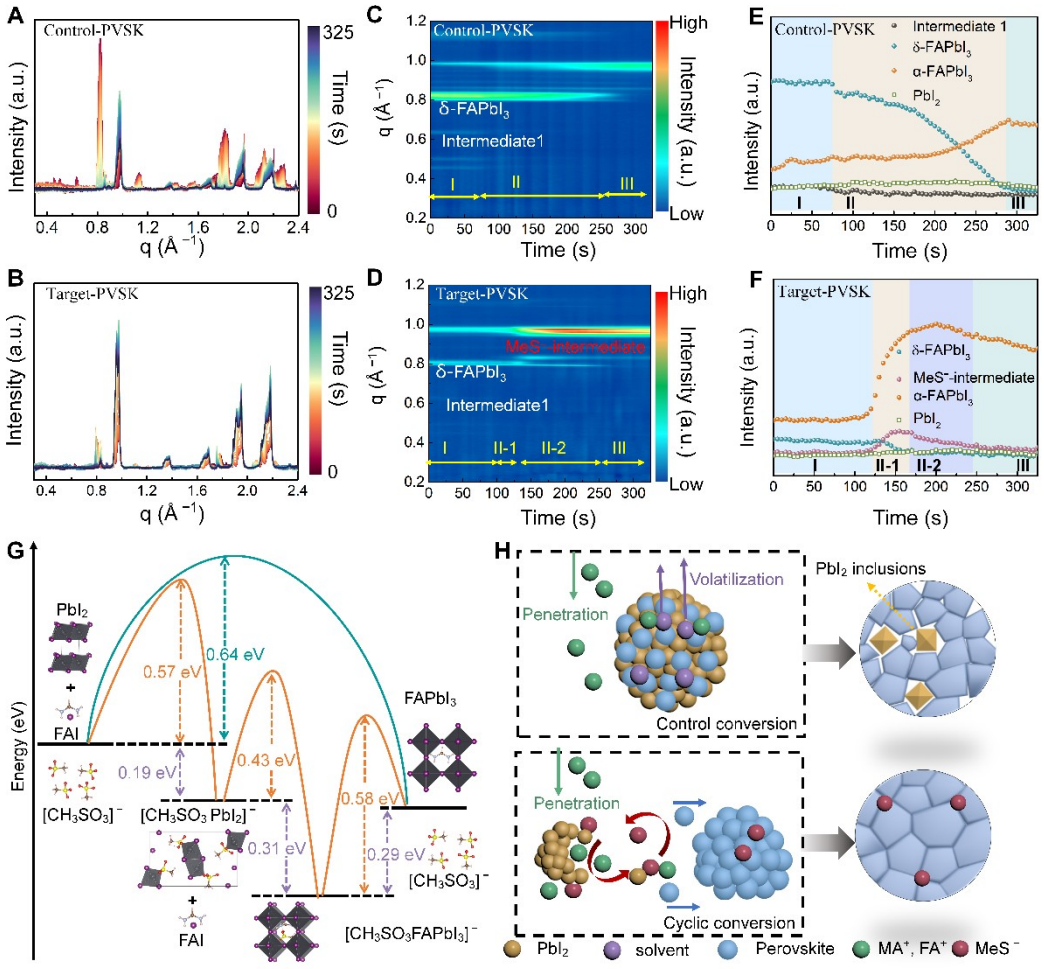

Figure 3. The perovskite conversion evolution analysis. (**A**-**F**) The in situ GIWAXS results of Control-PVSK (**A**, **C**, **E**) and Target-PVSK (**B**, **D**, **F**) films during the annealing process. (**A**, **B**) The integrated line profiles. (**C**, **D**) Corresponding false-color intensity mappings. (**E**, **F**) Time evolution in the peak intensity of the related

phases. (**G**) Free energy calculation for conversion of $FAPbI_3$ directly (teal solid) and with MeS^- (orange solid). (**H**) Schematic illustration of the conventional (control) and cyclic reaction pathway models.

2.4 Properties of perovskite films

High-angle annular dark-field scanning transmission electron microscopy (HAADF-STEM) images and corresponding energy disperse X-ray elemental mappings (EDX) were obtained to investigate the nanoscale compositional homogeneity of the resulting perovskite. The basic elements (Pb, I and N) of perovskite are present in cross section (Figure foaming reactionS17) and grain surface (Figure S18A and S18B) for both samples. It is noted that the S element (Figure 4A, 4B and Figure S18B) is present on the grains of Target-PVSK, while it is barely detected for Control-PVSK. The lack of a discernible signal for the 2D perovskite phase in Target-PVSK (Figure S18C) suggests that the presence of MeS^- did not lead to the formation of a 2D perovskite structure. Moreover, the Target-PVSK has a d-spacing of 3.43 Å, akin to that of Control-PVSK (3.41 Å). Coupled with the absence of a peak shift in the XRD results shown in Figure S14, we propose that MeS^- coordinates with the perovskite, indicating a uniform distribution within the perovskite film rather than entering the lattice to induce expansion. Combining with the emergence of C–S peak at 285.0 eV from C 1s and oxidized sulfur from S 2p of SRPES (Figure S19A and S19B)[35], we can speculate that the S in Target-PVSK originates from MeS^-. Furthermore, ToF-SIMS depth profiles in Figure 4C indicate that the diffusion depths of both the organic cations (including FA^+, MA^+) and halogen anions (I^-, Cl^-) are greater in Target-PVSK compared to Control-PVSK. This suggests that the subsequently applied ammonium salts can readily penetrate into the pre-formed PbI_2 via the multi-scale porous architecture. Figure S20A-D shows the topography and surface potential mapping of perovskite film measured by Kelvin probe force microscopy (KPFM). Target-PVSK shows lower roughness (R_q) and slightly higher average contact potential difference (CPD) values (R_q=11.55 nm, CPD=0.110 V) than that of Control-PVSK (R_q=16.72

nm, CPD=0.108 V). Visualized distributions of height and potential are provided in Figure S20E and S20F. These results suggest that the homogeneity of components in Target-PVSK has been improved due to the enhanced conversion.

To assess the nanoscopic structural homogeneity of perovskite, we conducted GIWAXS characterizations with different incidence angles. Figure 4C and 4D shows 2D GIWAXS patterns of perovskite films with and without MeSH at incidence angles of 0.05°, 0.40° and 1.00°, respectively. With increasing incidence angle, the peak intensity of the perovskite phase increases (Figure S21A, S21B and Table S1). Compared with the control group, the corresponding peak area ratio of PbI_2 to PVSK (Figure S21C) is reduced for the target group. We further calculated microstrain using the Williamson-Hall method (see Note S1)[36]. Target-PVSK has a smaller microstrain than the Control-PVSK (Figure S21D). The decrease in microstrain implies the potential suppression of asymmetric strain fields at grain boundaries induced by lattice distortions and inhomogeneities[37]. This reduction in microstrain can be attributed to the enhanced homogeneity facilitated by the catalyst-like system in Target-PVSK.

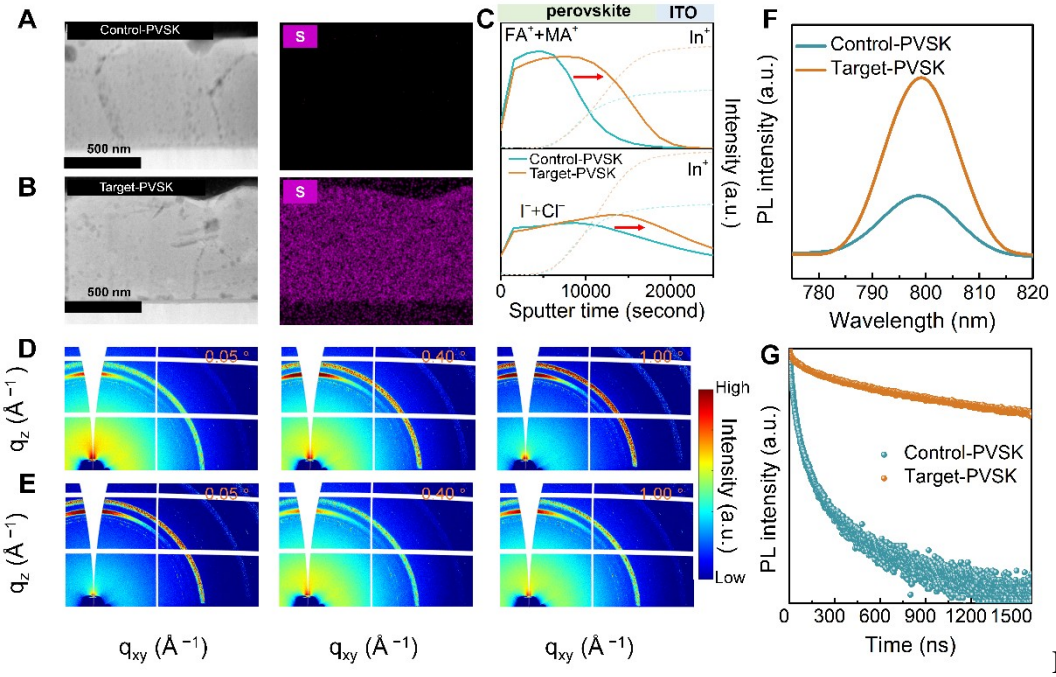

Figure 4. The composition and properties of perovskite films. The cross-sectional HAADF-STEM and corresponding EDX mappings for the ITO/SnO_2/perovskite samples: (**A**) Control-PVSK, (**B**) Target-PVSK. (**C**) ToF-SIMS results of Control-

PVSK and Target-PVSK on ITO substrates. The dotted line signifies the signal of In^+ from ITO. (**D**, **E**) The 2D GIWAXS patterns of Control-PVSK and Target-PVSK with incidence angles of 0.05°, 0.40° and 1.00°, respectively. (**F**, **G**) Corresponding steady-state PL spectra (**F**) and TRPL spectra (**G**) of Control-PVSK and Target-PVSK.

Compared with Control-PVSK, Target-PVSK generates stronger photoluminescence (PL) emission at 780 nm, consistent with its better crystal quality. Figure 4H and Table S2 show the time-resolved PL spectra and the results from bi-exponential fitting, respectively. Target-PVSK shows considerably larger τ_1 (37.42 ns vs. 13.63 ns) and τ_2 (234.78 ns vs. 83.79 ns), further verifying the reduced trap density of Target-PVSK[38]. We used transient absorption spectroscopy (TAS) to study the defect density and carrier lifetimes in Control-PVSK and Target-PVSK samples on quartz substrates (Figure S22). As shown in Figure S22, A-D, both samples showed a minimal difference in the photon bleaching peak positions, suggesting the impact from defects rather than compositional variations on dynamics[39]. The Target-PVSK sample displayed a longer decay time at 674.4 ps compared to the control with a decay time of 547.4 ps (see Note S2, Figure S22E and Table S3). This indicates a reduction in non-radiative recombination [39], consistent with the PL results in Figure 4F and 4G. The space charge-limited current (SCLC) data in Figure S23 reveals that the Target device has a lower trap-filled limit voltage (V_{TFL}) of 0.127 V compared to the Control device, with a V_{TFL} of 0.267 V, suggesting a reduced defect density in Target[40]. Combining the results of ultraviolet photoelectron spectroscopy (UPS) with the bandgap calculated from quantum efficiency data (Figure S24), the energy level diagram is resolved and shown in Figure S25. The valence band maximum (E_{VBM}) of Target-PVSK shows an upshift, reducing the injection barrier for hole transport from perovskite layer to the hole transport layer.

2.5 Photovoltaic performance of PSCs

A set of PSCs (FTO/SnO_2/PVSK/spiro-OMeTAD/Au) based on the resulting perovskite films were fabricated to examine photovoltaic performance. The current density-voltage (J–V) curves in Figure 5A and corresponding parameters in Table S4 are obtained under different scan directions. The MeSH-based device (denoted as Target) achieved the champion power conversion efficiency (PCE) of 24.45% under reverse scan (RS), with an open-circuit voltage (V_{OC}) of 1.169 V, a short circuit current density (J_{SC}) of 24.78 mA·cm^{-2} and a fill factor (FF) of 84.40%. This PCE surpassed that of the MeSH-free device (denoted as Control) having a PCE of 21.91%. The PCE of Target under forward scan (FS) is 23.62%, signifying a discernible mitigation of hysteresis, ascribed to a notable reduction in the residual PbI_2 content[41]. Moreover, Target had a higher stabilized PCE of 23.98% (Figure 5B), which was closer to the maximum PCE obtained from the J–V curves, demonstrating reduced hysteresis effects. The corresponding incident photon-electron conversion (IPCE) spectra and integrated current densities (J_{intes}) are shown in Figure 5C. The J_{intes} of Control and Target devices are 23.66 mA·cm^{-2} and 24.40 mA·cm^{-2}, respectively, in good agreement with the J_{SC}. The Target device demonstrates a remarkable and abrupt increase in EQE within the 750-830 nm range, while the absorption for Target-PVSK (Figure S26) shows only a slight increase in this range compared with its counterpart. This observation suggests that the enhanced EQE within this range could be due to the suppression of nonradiative interfacial recombination as a result of the enhanced quality of the perovskite film[42]. Figure 5D displays the statistics of a batch of 20 devices, clearly showing narrower distributions of performance parameters for Target devices, indicating improved reproducibility. Target displays a longer carrier lifetime (69.54 μs vs. 35.42 μs) from transient photovoltage (TPV) decays (Figure 5E) and higher built-in voltage (V_{bi}) of 1.01 V from the Mott-Schottky measurement (Figure S27), consistent with the enhanced V_{OC}[43].

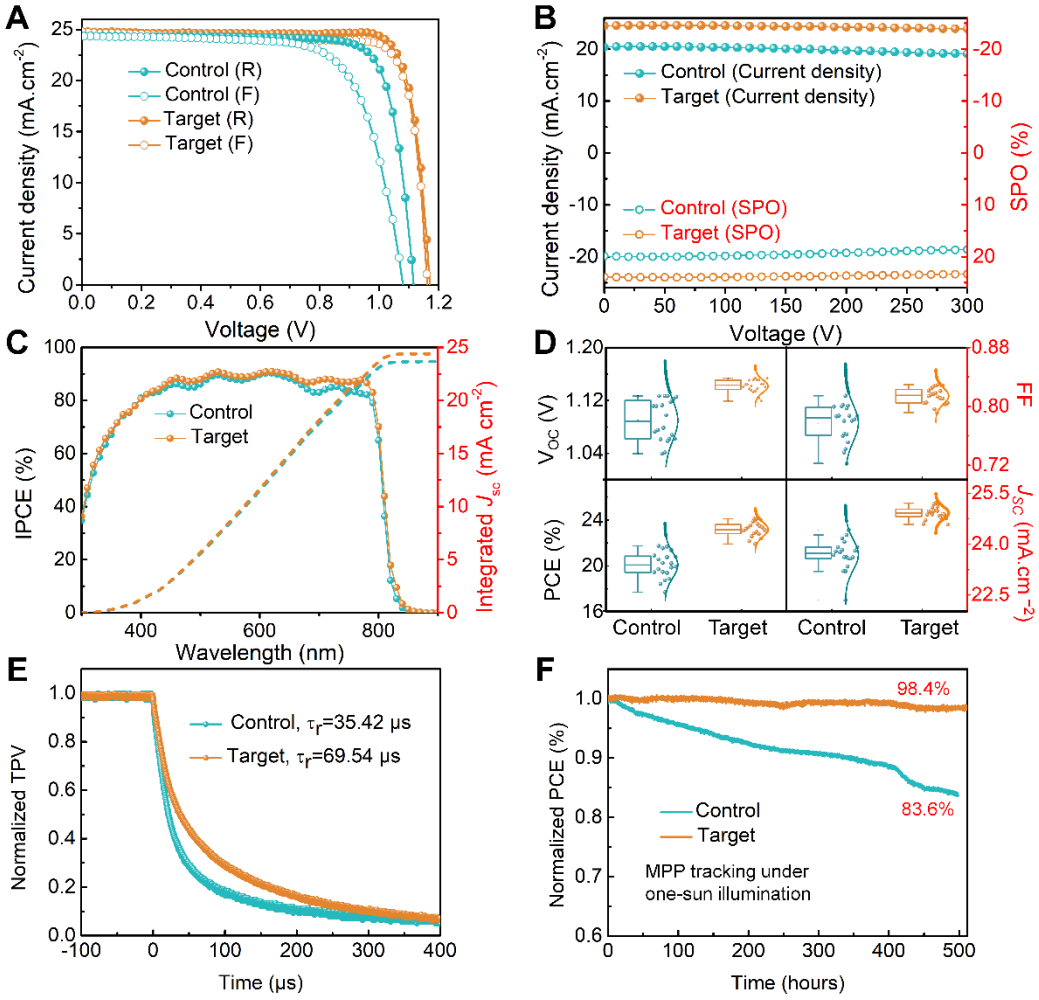

Figure 5. Photovoltaic performance and stability of devices. (**A**) *J*–*V* curves of photovoltaic devices obtained under reverse and forward scans. (**B**) Stable power outputs at the maximum power point (MPP). (**C**) IPCE spectrum and integrated photocurrent density. (**D**) The statistical distribution of photovoltaic performance parameters for a batch of 20 devices. (**E**) Normalized transient photovoltage (TPV) decay curves. (**F**) MPP tracking of unencapsulated devices under continuous illumination with exposure in an N_2 atmosphere.

We show the continuous maximum power point (MPP) tracking under operation conditions in Figure 5F. The efficiency of Target device retained 98.4% after 511 hours when that of Control device decreased to 83.6%. The long-term stability test of the unencapsulated devices was also conducted under dark condition in ambient air

with a relative humidity (RH) of 30% and a temperature of 25 ℃ (Figure S28). The PCE of Target maintains 91% of its original value after 2016 hours, whereas the PCE of Control drops to 47% of its initial value. The enhanced storage stability of the MeSH-based device can be attributed to the improved nanoscale homogeneity, which effectively suppresses the decomposition of the perovskite material.

3. Conclusion

In summary, we introduced a cyclic conversion pathway to target the structural and compositional inhomogeneities of perovskite. The occurrence of the catalytic reaction was attributed to a nonvolatile foaming agent (MeSH), which created a multi-scale porous PbI_2 architecture bonding with remaining MeS^- ions that acted like catalysts involving in perovskite conversion. The validity of this mechanism was confirmed through the application of advanced scattering and imaging techniques, allowing for the characterization of temporal and spatial resolutions. The reduced activation energy for MeS^- based conversion was corroborated by density functional theory (DFT) calculations. The improved homogeneity enabled superior optoelectronic properties, inducing PSCs with simultaneously high performance and long-term stability over 2000 hours. Our results provide a new insight for fabricating efficient and stable optoelectronic devices using catalysts.

Supporting Information

Supporting Information is available from the Wiley Online Library or from the author.

Acknowledgements

We thank beamlines BL19U1, BL17B1 and BL14B1 at the SSRF for providing the beamtime and User Experiment Assist System of SSRF for their help. We acknowledge beamline BL11U and the Catalysis and Surface Science Endstation of the NSRL for the provision of experimental facilities and help. We would like to thank Prof. Shibing Long, Dr. Jiajiu Ye, Prof. Fengjia Fan and Zidu Li for the

suggestion on experiments and the paper and the characterization of MPP tracking and TAS, respectively. This work was financially supported by the National Natural Science Foundation of China (62104221, 51972123, 61805138, U1705256, 52203208), the Fundamental Research Funds for the Central Universities (WK2100000025), USTC Research Funds of the Double First-Class Initiative (YD2100002007), USTC National Synchrotron Radiation Laboratory (KY2190000002), Beijing Natural Science Foundation (JQ21005), the National Key R&D Program of China (2021YFB3800100, 2021YFB3800101), the China Postdoctoral Science Foundation (2020M670036) and the R&D Fruit Fund (20210001). This work was also sponsored by Beijing Nova Program. Y.Q.Y. thanks China and Germany Exchange Postdoctoral Program for financial support. This work was partially carried out at the USTC Center for Micro and Nanoscale Research and Fabrication. Y.Q.Y., G.L., and L.Z. contributed equally to this work. Q.H., Y.Q.Y. and Y.L. conceived the idea. Y.Q.Y., Q.H., J.W. and Y.L. designed all the experiments. Y.Q.Y. conducted the experiments including fabrication and film and device characterization. G.L. and C.D. contributed to the characterization J_{SC}-V_{OC} curves and Mott-Schottky measurements. P.Y.T., H.L. and L.T. prepared samples and carried out the characterization of the HTEM and EDX mapping. J_{SC}-V_{OC} curves and Mott-Schottky measurements. L.Z., Y.G.Y. and S.L. prepared the film samples and carried out GIWAXS characterizations, and L.Z. processed and analysed the GIWAXS data. Q.L. and L.Z. performed the AFM-KPFM and analysed the results. P.J.T., C.Y., L.C. and Y.G. conducted and interpreted the nano CT measurements. J.S. and C.H. contributed to the ToF-SIMS measurements, and C.H. and L.Z. analysed the data. P.T.J., J.Z. and H.D. conducted the SRPES characterizations. L.T., S.W. and Z.Z. performed the NMR, TPV and trap density measurements. H.Q. and J.W. supervised the project. Y.L. and P.Y.T. gave suggestions and comments. Y.Q.Y. wrote the draft of manuscript. Y.L., L.Z., G.L., A.A., Q.H. and P.J.T. revised the paper. All the authors discussed the results and commented on the paper.

Conflict of Interest

The authors declare no conflict of interest.

References:

[1] G. Xing, N. Mathews, S. Sun, S. S. Lim, Y. M. Lam, M. Grätzel, S. Mhaisalkar, T. C. Sum, Science 2013, 342, 344; C. Wehrenfennig, G. E. Eperon, M. B. Johnston, H. J. Snaith, L. M. Herz, Advanced materials 2014, 26, 1584; L. Dou, Y. M. Yang, J. You, Z. Hong, W.-H. Chang, G. Li, Y. Yang, Nature communications 2014, 5, 1; D. Zhang, Q. Zhang, B. Ren, Y. Zhu, M. Abdellah, Y. Fu, B. Cao, C. Wang, L. Gu, Y. Ding, Nature Photonics 2022, 16, 284.

[2] W. Nie, H. Tsai, R. Asadpour, J.-C. Blancon, A. J. Neukirch, G. Gupta, J. J. Crochet, M. Chhowalla, S. Tretiak, M. A. Alam, Science 2015, 347, 522.

[3] K. Zhang, Z. Wang, G. Wang, J. Wang, Y. Li, W. Qian, S. Zheng, S. Xiao, S. Yang, Nature communications 2020, 11, 1.

[4] T. Bu, J. Li, H. Li, C. Tian, J. Su, G. Tong, L. K. Ono, C. Wang, Z. Lin, N. Chai, Science 2021, 372, 1327.

[5] T. A. S. Doherty, A. J. Winchester, S. Macpherson, D. N. Johnstone, V. Pareek, E. M. Tennyson, S. Kosar, F. U. Kosasih, M. Anaya, M. Abdi-Jalebi, Z. Andaji-Garmaroudi, E. L. Wong, J. Madéo, Y.-H. Chiang, J.-S. Park, Y.-K. Jung, C. E. Petoukhoff, G. Divitini, M. K. L. Man, C. Ducati, A. Walsh, P. A. Midgley, K. M. Dani, S. D. Stranks, Nature 2020, 580, 360.

[6] S. Macpherson, T. A. Doherty, A. J. Winchester, S. Kosar, D. N. Johnstone, Y.-H. Chiang, K. Galkowski, M. Anaya, K. Frohna, A. N. Iqbal, Nature 2022, 607, 294.

[7] K. Frohna, M. Anaya, S. Macpherson, J. Sung, T. A. Doherty, Y.-H. Chiang, A. J. Winchester, K. W. Orr, J. E. Parker, P. D. Quinn, Nature Nanotechnology 2022, 17, 190.

[8] E. M. Tennyson, T. A. Doherty, S. D. Stranks, Nature Reviews Materials 2019, 4, 573.

[9] H. Chen, Advanced Functional Materials 2017, 27, 1605654; A. Sharenko, M. F. Toney, Journal of the American Chemical Society 2016, 138, 463.

[10] T. Liu, Q. Hu, J. Wu, K. Chen, L. Zhao, F. Liu, C. Wang, H. Lu, S. Jia, T. Russell, Advanced Energy Materials 2016, 6, 1501890.

[11] H. Zeng, L. Li, F. Liu, M. Li, S. Zhang, X. Zheng, L. Luo, S. You, Y. Zhao, R. Guo, Advanced Energy Materials 2022, 12, 2102820.

[12] P. Ahlawat, A. Hinderhofer, E. A. Alharbi, H. Lu, A. Ummadisingu, H. Niu, M. Invernizzi, S. M. Zakeeruddin, M. I. Dar, F. Schreiber, Science Advances 2021, 7, eabe3326.

[13] B.-w. Park, H. W. Kwon, Y. Lee, D. Y. Lee, M. G. Kim, G. Kim, K.-j. Kim, Y. K. Kim, J. Im, T. J. Shin, Nature Energy 2021, 6, 419.

[14] Y. Deng, C. H. Van Brackle, X. Dai, J. Zhao, B. Chen, J. Huang, Science advances 2019, 5, eaax7537; G. E. Eperon, V. M. Burlakov, P. Docampo, A. Goriely, H. J. Snaith, Advanced functional materials 2014, 24, 151.
[15] Y. Wu, A. Islam, X. Yang, C. Qin, J. Liu, K. Zhang, W. Peng, L. Han, Energy & Environmental Science 2014, 7, 2934.
[16] H. Zhang, J. Mao, H. He, D. Zhang, H. L. Zhu, F. Xie, K. S. Wong, M. Grätzel, W. C. Choy, Advanced Energy Materials 2015, 5, 1501354.
[17] J. V. Passarelli, C. M. Mauck, S. W. Winslow, C. F. Perkinson, J. C. Bard, H. Sai, K. W. Williams, A. Narayanan, D. J. Fairfield, M. P. Hendricks, Nature chemistry 2020, 12, 672; Y. C. Wang, J. Chang, L. Zhu, X. Li, C. Song, J. Fang, Advanced Functional Materials 2018, 28, 1706317.
[18] C. H. Chen, Y. H. Lou, K. L. Wang, Z. H. Su, C. Dong, J. Chen, Y. R. Shi, X. Y. Gao, Z. K. Wang, Advanced Energy Materials 2021, 11, 2101538.
[19] W. Hui, L. Chao, H. Lu, F. Xia, Q. Wei, Z. Su, T. Niu, L. Tao, B. Du, D. Li, Science 2021, 371, 1359.
[20] C. Luo, Y. Zhao, X. Wang, F. Gao, Q. Zhao, Advanced Materials 2021, 33, 2103231.
[21] J. Jeong, J. Yang, C.-S. Ha, W.-J. Cho, I. Chung, Polymer bulletin 2012, 68, 1227.
[22] J. C. Caicedo, A. Goodman, K. W. Karhohs, B. A. Cimini, J. Ackerman, M. Haghighi, C. Heng, T. Becker, M. Doan, C. McQuin, Nature methods 2019, 16, 1247.
[23] L. Pe, F. Xu, K. L. Hohn, J. Li, D. Wang, Journal of Biomaterials and Nanobiotechnology 2014, 5, 8.
[24] L. Kong, X. Zhang, Y. Li, H. Wang, Y. Jiang, S. Wang, M. You, C. Zhang, T. Zhang, S. V. Kershaw, Nature communications 2021, 12, 1246.
[25] J. Jeong, T. Kim, W. J. Cho, I. Chung, Polymer international 2013, 62, 1094; S. Mukhopadhyay, M. Zerella, A. T. Bell, in *Studies in Surface Science and Catalysis*, Vol. 147 (Eds: X. Bao, Y. Xu), Elsevier, 2004, 523.
[26] X. Li, M. Ibrahim Dar, C. Yi, J. Luo, M. Tschumi, S. M. Zakeeruddin, M. K. Nazeeruddin, H. Han, M. Grätzel, Nature chemistry 2015, 7, 703.
[27] C. Sun, Y. Zhang, P. Wang, Y. Yang, Y. Wang, J. Xu, Y. Wang, W. W. Yu, Nanoscale research letters 2016, 11, 1.
[28] C. Li, Q. Guo, H. Zhang, Y. Bai, F. Wang, L. Liu, T. Hayat, A. Alsaedi, Z. a. Tan, Nano Energy 2017, 40, 248.
[29] Q. Hu, L. Zhao, J. Wu, K. Gao, D. Luo, Y. Jiang, Z. Zhang, C. Zhu, E. Schaible, A. Hexemer, Nature communications 2017, 8, 1.
[30] M. Qin, H. Xue, H. Zhang, H. Hu, K. Liu, Y. Li, Z. Qin, J. Ma, H. Zhu, K. Yan, Advanced materials 2020, 32, 2004630.
[31] C. Li, Q. Guo, H. Zhang, Y. Bai, F. Wang, L. Liu, T. Hayat, A. Alsaedi, Z. a. Tan, Nano Energy 2017, 40, 248.
[32] M. Li, R. Sun, J. Chang, J. Dong, Q. Tian, H. Wang, Z. Li, P. Yang, H. Shi, C. Yang, Nature Communications 2023, 14, 573.

[33] X. Du, J. Zhang, H. Su, X. Guo, Y. Hu, D. Liu, N. Yuan, J. Ding, L. Gao, S. Liu, Advanced Materials 2022, 34, 2204098.
[34] V. L. Pool, B. Dou, D. G. Van Campen, T. R. Klein-Stockert, F. S. Barnes, S. E. Shaheen, M. I. Ahmad, M. F. Van Hest, M. F. Toney, Nature communications 2017, 8, 1.
[35] T. C. Tudino, R. S. Nunes, D. Mandelli, W. A. Carvalho, Frontiers in Chemistry 2020, 8, 263.
[36] W. Li, S. Sidhik, B. Traore, R. Asadpour, J. Hou, H. Zhang, A. Fehr, J. Essman, Y. Wang, J. M. Hoffman, Nature nanotechnology 2022, 17, 45.
[37] T. A. Doherty, A. J. Winchester, S. Macpherson, D. N. Johnstone, V. Pareek, E. M. Tennyson, S. Kosar, F. U. Kosasih, M. Anaya, M. Abdi-Jalebi, Nature 2020, 580, 360.
[38] G. Yang, Z. Ren, K. Liu, M. Qin, W. Deng, H. Zhang, H. Wang, J. Liang, F. Ye, Q. Liang, Nature Photonics 2021, 15, 681.
[39] W. Chen, Y. Wang, G. Pang, C. W. Koh, A. B. Djurišić, Y. Wu, B. Tu, F. z. Liu, R. Chen, H. Y. Woo, Advanced Functional Materials 2019, 29, 1808855.
[40] D. Shi, V. Adinolfi, R. Comin, M. Yuan, E. Alarousu, A. Buin, Y. Chen, S. Hoogland, A. Rothenberger, K. Katsiev, Y. Losovyj, X. Zhang, P. A. Dowben, O. F. Mohammed, E. H. Sargent, O. M. Bakr, Science 2015, 347, 519.
[41] L. Zhao, Q. Li, C.-H. Hou, S. Li, X. Yang, J. Wu, S. Zhang, Q. Hu, Y. Wang, Y. Zhang, Y. Jiang, S. Jia, J.-J. Shyue, T. P. Russell, Q. Gong, X. Hu, R. Zhu, Journal of the American Chemical Society 2022, 144, 1700.
[42] X. Ma, X. Shai, X. Li, J. Sun, W. Chen, Q. Zhou, D. He, H. Yang, J. Chen, Solar RRL, n/a, 2300495.
[43] D. Wu, W. Li, H. Liu, X. Xiao, K. Shi, H. Tang, C. Shan, K. Wang, X. W. Sun, A. K. K. Kyaw, Advanced Science 2021, 8, 2101729.